PNAS

Supporting Information for

Stress-dependent activation entropy in thermally activated cross-slip of dislocations

Yifan Wang and Wei Cai

Corresponding Author Wei Cai.
E-mail: caiwei@stanford.edu

This PDF file includes:

Supporting text
Figs. S1 to S6
Table S1
SI References

Supporting Information Text

I. Correction to the soft vibrational modes

The harmonic transition state theory (HTST) described in Eq. 3 only applies when all the relevant phonon modes appear to be harmonic oscillators ($3N - 3$ modes for the initial state A, and $3N - 4$ for the saddle state S). However, besides the three rigid-body translational modes for both states A and S, and the imaginary mode along the reaction coordinate direction for state S, there are two soft vibrational modes that cannot be approximated by harmonic oscillators for a single dislocation cross-slip process. One mode is the constriction of the partials moves along the dislocation line (Goldstone mode) for the saddle state S, and another mode is the entire dislocation moves along the gliding direction on the original slip plane (Gliding mode) for the initial state A. This section discusses the theoretical and numerical treatments of these two soft vibrational modes that correct the rate predicted by HTST.

Fig. S1(a) shows the Goldstone mode of the saddle state S, in which the constriction can move along the dislocation line direction. To obtain the energy profile along the Goldstone mode, we start from the atomic configuration of transition state S, as shown in Fig. 1A. We first move all the atoms along the dislocation line direction by one Burger's vector magnitude b to obtain the next repeated configuration. Now the atoms away from the dislocation core are overlapping with their next repeated neighbor, while the atoms in the dislocation core are moved slightly ($\ll b$) away from their next neighbor, due to the motion of the constriction. The atom IDs are then reassigned to these closest next neighbors, so that effectively only the constriction is moved by b along the dislocation line direction. Note that although this new configuration S' effectively moves the constriction by b, most of the atoms have not moved. The atoms away from the dislocation core are not moved while the motion of the atoms in the dislocation core is much smaller than b. The energy profile of the Goldstone mode is then obtained by linear interpolation between states S and S', shown as a solid line in Fig. S1(b), with its harmonic approximation of the local minimum illustrated as the dashed line.

On the one hand, it is readily seen that the Goldstone mode in cross-slip process has a non-zero stiffness. Hence, this mode cannot be simply excluded from the Hessian matrix as a 4th zero-frequency mode (after the three rigid-body translation modes) like in SI Ref. (1). On the other hand, it can be seen that the actual energy profile is significantly deviating from the harmonic approximation that is accounted for in the HTST. Therefore, we correct the HTST rate by multiplying a factor $\tilde{\nu}_S$, which can be written as the ratio between the partition functions of the 1D energy profile ($^{\mathrm{G}}$) and the harmonic approximation ($^{\mathrm{H}}$),

$$\tilde{\nu}_{\mathrm{S}} = \frac{z_{\mathrm{S}}^{\mathrm{H}}}{z_{\mathrm{S}}^{\mathrm{G}}} = \frac{\int_{-\infty}^{\infty} \exp[-E_{\mathrm{S}}^{\mathrm{H}}(x)/k_{\mathrm{B}}T]\,\mathrm{d}x}{N_{\mathrm{x}} \int_{-R/2}^{R/2} \exp[-E_{\mathrm{S}}^{\mathrm{G}}(x)/k_{\mathrm{B}}T]\,\mathrm{d}x} = \frac{b}{L_{\mathrm{x}}} \frac{\sqrt{2\pi k_{\mathrm{B}}T/K}}{\int_{-R/2}^{R/2} \exp[-E_{\mathrm{S}}^{\mathrm{G}}(x)/k_{\mathrm{B}}T]\,\mathrm{d}x} \tag{10}$$

where K is the stiffness(curvature) of the harmonic approximation at $x = 0$, indicated by the dashed quadratic curve in Fig. S1(b). R is the total atom displacement of one period, in which the constriction effectively moves by a Burger's vector b along the dislocation line direction (See Fig. S2). Note that Fig. S1(b) only shows one period of $E_{\mathrm{S}}^{\mathrm{G}}$, since the lattice in the $[1\bar{1}0]$ direction is repeated for $N_{\mathrm{x}} = L_x/b$ times in the dislocation line direction, as shown in Fig. S2. The denominator is evaluated by numerical integration of the energy profile $E_{\mathrm{S}}^{\mathrm{G}}(r)$ illustrated as the solid curve. The correction factor for $300\,\mathrm{K}$ is evaluated as $\tilde{\nu}_S \sim 0.15$, contributing about one-order-of-magnitude error to the rate prediction.

Similarly, the gliding mode of the initial state is shown in Fig. S1(c). We move the dislocation along the gliding direction by one gliding vector $\boldsymbol{h} = \frac{a}{6}[\bar{1}\bar{1}2]$ to obtain the next repeated configuration A'. To achieve this, the atoms are first moving along the repeated lattice direction along the zig-zag line direction as shown in Fig. S2, so that the atoms are close to their next neighbor. The atom IDs are then reassigned to their closest next neighbor, so that only the atoms near the dislocation core are moved and effectively the dislocation is moved by h in the gliding direction. The energy profile of gliding is then obtained by MEP search, as shown in Fig. S1(d). It is readily seen that the energy barrier is much higher than the Goldstone mode, and the harmonic approximation is working better estimating the partition function compared to the Goldstone mode. The correcting factor of the gliding mode $\tilde{\nu}_A$ can be written as,

$$\tilde{\nu}_{\mathrm{A}} = \frac{z_{\mathrm{A}}^{\mathrm{H}}}{z_{\mathrm{A}}^{\mathrm{Gl}}} = \frac{\int_{-\infty}^{\infty} \exp[-E_{\mathrm{A}}^{\mathrm{H}}(z)/k_{\mathrm{B}}T]\,\mathrm{d}z}{\int_{-R/2}^{R/2} \exp[-E_{\mathrm{A}}^{\mathrm{Gl}}(z)/k_{\mathrm{B}}T]\,\mathrm{d}z} = \frac{\sqrt{2\pi k_{\mathrm{B}}T/K_{\mathrm{A}}}}{\int_{-R/2}^{R/2} \exp[-E_{\mathrm{A}}^{\mathrm{Gl}}(z)/k_{\mathrm{B}}T]\,\mathrm{d}z} \tag{11}$$

where K_A is the curvature of the harmonic approximation. The correction factor $\tilde{\nu}_A$ is estimated around ~ 1.3 at $300\,\mathrm{K}$, indicating that the harmonic approximation is pretty good in estimating the partition function of the gliding mode. It is worth noting that the gliding mode does not need to multiply by the number of repeat lattices N_z in the z-direction. The reason is that while the dislocation can cross-slip from any of the N_z equivalent locations on the original slip plane, for each one of these equivalent configurations of the initial state A, there is a set of N_x saddle configurations corresponding to the saddle state S. In total, state S has $N_x N_z$ equivalent sites while state A has N_z equivalent sites. Therefore, the N_z factor is canceled and only an N_x factor need to be multiplied in calculating the Goldstone mode. This is consistent with the fact that the cross-slip rate is proportional to the dislocation line length (N_x) but is independent from the length of the simulation cell in the gliding direction (N_z).

These two vibrational soft modes are accounted for by numerically evaluating the partition function based on their energy profile. Their effect can be significant, for example, the correction factor $\tilde{\nu}_{\mathrm{A}}/\tilde{\nu}_{\mathrm{S}} \approx 0.2$ under $\boldsymbol{\tau}_{\mathrm{app}} = (-0.6, -0.8, 0.8)\mathrm{GPa}$ and at

300 K. We believe that these two terms in the prefactor $\nu_0(\varepsilon) = \nu_{\text{HTST}} \, \tilde{\nu}_\text{A}/\tilde{\nu}_\text{S}$ cover all the important vibrational contribution to the free energy difference $F_\text{c}(\varepsilon)$.

II. Additional calculations for different applied stresses

To assess the generality of the conclusions, we repeat the MD simulations and MEP calculations for cross-slip at two different applied stress conditions of $\boldsymbol{\tau}_{\text{app}} = (-0.8, -0.8, 0.8)\text{GPa}$ and $\boldsymbol{\tau}_{\text{app}} = (-0.8, -0.8, 0.6)\text{GPa}$, as shown in Fig. S3. After using the finite-temperature strain $\boldsymbol{\varepsilon}_T$ to calculate the activation energy, the HTST estimate (blue squares) of the cross-slip rate matches with the MD results (orange stars) for different applied stress conditions. This result indicates that the thermal expansion and the thermal softening effects contribute primarily to the large activation entropy at a given applied stress. The activation entropy S_c is evaluated as the negative slope of the activation energy decrease with increasing temperature.

To examine the stress-dependence of the activation entropy S_c described in Eq. 18, we perform the MEP calculations of 27 applied stress conditions, where the three shear stress components $-\sigma_\text{e}^\text{g}$, $-\sigma_\text{s}^\text{c}$, and σ_e^c varies among 0.0, 0.4, 0.8 GPa. The calculated activation entropy is marked as solid markers in Fig. 3, as a function of the effective shear stress τ^* from Eq. 15. It is readily seen that the activation entropy can be grouped into three curves by the value of σ_s^c. These stress-dependent activation entropy values are then modeled by Eq. 6(SI Text V) and shown as dashed lines in Fig. 3.

III. Constant-strain activation entropy from HTST

Based on TST, the cross-slip rate can be written as a function of constant strain $\boldsymbol{\varepsilon}$ and temperature T (2),

$$r_{\text{TST}}(\boldsymbol{\varepsilon}, T) = \frac{k_\text{B}T}{h} \, \exp\left[-\frac{F_\text{c}(\boldsymbol{\varepsilon}, T)}{k_\text{B}T}\right] = \frac{k_\text{B}T}{h} \, \exp\left[\frac{S_\text{c}(\boldsymbol{\varepsilon})}{k_\text{B}}\right] \exp\left[-\frac{E_\text{c}(\boldsymbol{\varepsilon})}{k_\text{B}T}\right] \tag{12}$$

where $F_\text{c} = F_S - F_A$ is the activation Helmholtz free energy, the free energy difference between the transition state S and initial state A. The activation Helmholtz free energy can be expressed as $F_\text{c}(\boldsymbol{\varepsilon}, T) = E_\text{c}(\boldsymbol{\varepsilon}) - TS_\text{c}(\boldsymbol{\varepsilon})$, where E_c and S_c are the activation energy and activation entropy as functions of strain $\boldsymbol{\varepsilon}$, respectively (2). Combining Eq. 4 and Eq. 12, the activation entropy can be obtained from HTST calculation,

$$S_\text{c} = k_\text{B} \ln\left(\nu_{\text{HTST}} \, \frac{\tilde{\nu}_\text{A}}{\tilde{\nu}_\text{S}} \frac{h}{k_\text{B}T}\right) \tag{13}$$

IV. Analytical expressions for stress-dependent activation enthalpy H_c

As we discussed in the main text (Fig. 3), the activation energy at finite temperature strain is equivalent to the activation enthalpy at zero temperature with excess stress applied. Since the MEP search algorithm is computationally expensive, it is not possible to calculate activation enthalpy everytime with a new applied stress condition. In this section, we will build an analytical formula for the activation enthalpy as a function of applied stress. Kuykendall et al. (3) and Esteban-Manzanares et al. (4) studied the zero-temperature stress-dependence of the cross-slip activation enthalpy, but the isotropic stress $-\hat{\sigma}\mathbf{I}$ is not considered in both works. Here we develop an H_c function based on Kuykendall et al. (2020)'s (3) expression, considering the applied Escaig-Schmid stress components $\boldsymbol{\tau}_{\text{app}} = (\sigma_\text{e}^\text{g}, \sigma_\text{s}^\text{c}, \sigma_\text{e}^\text{c})$ and the isotropic stress $\hat{\sigma}$:

$$H_\text{c}(\tau^*, \hat{\tau}_0) = A\left[1 - \left(\frac{\tau^*}{\hat{\tau}_0}\right)^p\right]^q \tag{14}$$

where the effective shear stress τ^* and the effective cross-slip stress $\hat{\tau}_0$ (where the energy barrier is zero) are defined as,

$$\tau^*(\sigma_\text{e}^\text{g}, \sigma_\text{e}^\text{c}, \sigma_\text{s}^\text{c}) = C_\text{e}^\text{g}\sigma_\text{e}^\text{g} + C_\text{e}^\text{c}\sigma_\text{e}^\text{c} + (D_\text{s}^\text{c}\sigma_\text{s}^\text{c})^2 \tag{15}$$

$$\hat{\tau}_0(-\hat{\sigma}, \sigma_\text{s}^\text{c}) = \tau_0 - K_1(-\hat{\sigma})(\sigma_\text{s}^\text{c})^2 - K_2(-\hat{\sigma})^{K_3} \tag{16}$$

We fit this expression based on $500(5 \times 5 \times 5 \times 4)$ MEP calculations, with $-\sigma_\text{e}^\text{g}$, $-\sigma_\text{s}^\text{c}$, and σ_e^c varies among 0.0, 0.2, 0.4, 0.6, and 0.8 GPa, and the hydrostatic stress $-\hat{\sigma}$ varies among 0.0, 2.0, 4.0, and 6.0 GPa. In these simulations, σ_e^g is negative (when it is non-zero), to promote constriction of the stacking fault, while σ_e^c is positive (when it is non-zero) to promote expansion of the stacking fault on the cross-slip plane. In our simulations, σ_s^c is negative (when it is non-zero), though both positive and negative Schmid stresses on the cross-slip plane are expected to promote cross-slip. Each MEP relaxation is performed for 800 iterations (which takes 8 hours on 32 cores) and is considered converged if (1) the slope of the linear fit of energy barrier over the last 400 steps is less than 10^{-5} eV/step; and (2) the mean squared error of the linear fit is less than 10^{-3} eV^2. If convergence is not reached, the MEP relaxation is restarted for another 400 iterations. If the energy barrier during relaxation becomes negative, we consider the calculation has failed to converge. All these 500 simulations (whose initial paths are constructed based on the FE mechanism) converge to MEPs that are consistent with the FE mechanism.

The fitted numerical values for the seven fitting parameters $(A, p, q, \tau_0, C_\mathrm{e}^\mathrm{g}, C_\mathrm{e}^\mathrm{c}, D_\mathrm{s}^\mathrm{c})$ are given in Table S1. It is worth noting that except for the magnitude A due to the smaller simulation cell in this work, the values of the parameters are the same as Kuykendall et al. (2020) (3), indicating the consistency of this analytical expression. Fig. S4 shows the fitted activation enthalpy as a function of τ^* and $\hat{\tau}_0$. The formula accurately predicts the activation enthalpy at any given applied stress $\tilde{\boldsymbol{\sigma}}$ within the fitting range.

V. Analytical expressions for stress-dependent activation entropy S_c

The activation entropy S_c is defined as the reduction of activation energy with increasing temperature and fixed stress condition $\boldsymbol{\sigma} = \boldsymbol{\tau}_\mathrm{app}$. Using Legendre transformation, the activation energy as a function of strain can be written in terms of activation enthalpy as a function of stress, i.e., $E_\mathrm{c}(\boldsymbol{\varepsilon}_T) = H_\mathrm{c}(\tilde{\boldsymbol{\sigma}})$. Here the $\tilde{\boldsymbol{\sigma}}$ is the corresponding stress for the finite-temperature strain $\boldsymbol{\varepsilon}_T$ at $0\,\mathrm{K}$, i.e., $\tilde{\boldsymbol{\sigma}} = \boldsymbol{\sigma}(\boldsymbol{\varepsilon}_T, 0\,\mathrm{K})$, where $\boldsymbol{\varepsilon}_T = \boldsymbol{\varepsilon}(\boldsymbol{\tau}_\mathrm{app}, T)$ is the finite-temperature strain. At $0\,\mathrm{K}$, excess stresses need to be applied for the system to remain the strain $\boldsymbol{\varepsilon}_T$, as shown in Fig. S5(b)(c),

$$\tilde{\boldsymbol{\sigma}} = \hat{\sigma}\mathbf{I} + \boldsymbol{\tau} = \boldsymbol{\tau}_\mathrm{app} + \hat{\sigma}\mathbf{I} + \boldsymbol{\tau}_\mathrm{ex} \tag{17}$$

where $\hat{\sigma}\mathbf{I}$ is the excess isotropic stress and $\boldsymbol{\tau}_\mathrm{ex}$ is the excess shear stress. As a result, the activation entropy can be decomposed as,

$$
\begin{aligned}
S_\mathrm{c} &= \left(\frac{\partial E_\mathrm{c}(\boldsymbol{\varepsilon}_T)}{\partial T}\right)_{\boldsymbol{\sigma}=\boldsymbol{\tau}_\mathrm{app}} = \left(\frac{\partial H_\mathrm{c}(\tilde{\boldsymbol{\sigma}})}{\partial T}\right)_{\boldsymbol{\tau}_\mathrm{app}} \\
&= \left(\frac{\partial H_\mathrm{c}}{\partial \tilde{\boldsymbol{\sigma}}}\right)\left(\frac{\partial \tilde{\boldsymbol{\sigma}}}{\partial \boldsymbol{\varepsilon}_T}\right)\left(\frac{\partial \boldsymbol{\varepsilon}_T}{\partial T}\right)_{\boldsymbol{\tau}_\mathrm{app}}
\end{aligned} \tag{18}
$$

where the first term $(\partial H_\mathrm{c}/\partial \tilde{\boldsymbol{\sigma}})$ is the stress gradient of the activation enthalpy, which can be calculated from the analytical expression Eq. 14, 15, and 16 in the previous section. The second term $(\partial \tilde{\boldsymbol{\sigma}}/\partial \boldsymbol{\varepsilon}_T)$ comes from the constitutive relationship at $0\,\mathrm{K}$. The last term $(\partial \boldsymbol{\varepsilon}_T/\partial T)_{\boldsymbol{\sigma}=\boldsymbol{\tau}_\mathrm{app}}$ is the strain change with increasing temperature given the system remains at the applied stress $\boldsymbol{\tau}_\mathrm{app}$, as shown in Fig. S5(b)(c). This entropic effect can be further decomposed according to the isotropic component and the shear component of the stress,

$$
\begin{aligned}
S_\mathrm{c} &= \left[\left(\frac{\partial H_\mathrm{c}}{\partial(-\hat{\sigma})}\right)\left(\frac{\partial(-\hat{\sigma})}{\partial \boldsymbol{\varepsilon}_T}\right) + \left(\frac{\partial H_\mathrm{c}}{\partial \boldsymbol{\tau}}\right)\left(\frac{\partial \boldsymbol{\tau}}{\partial \boldsymbol{\varepsilon}_T}\right)\right]\left(\frac{\partial \boldsymbol{\varepsilon}_T}{\partial T}\right)_{\boldsymbol{\tau}_\mathrm{app}} \\
&= \left(\frac{\partial H_\mathrm{c}}{\partial(-\hat{\sigma})}\right)\left[\left(\frac{\partial(-\hat{\sigma})}{\partial \boldsymbol{\varepsilon}_T}\right)\left(\frac{\partial \boldsymbol{\varepsilon}_T}{\partial T}\right)_{\boldsymbol{\tau}_\mathrm{app}}\right] + \left(\frac{\partial H_\mathrm{c}}{\partial \boldsymbol{\tau}}\right)\left[\left(\frac{\partial \boldsymbol{\tau}}{\partial \boldsymbol{\varepsilon}_T}\right)\left(\frac{\partial \boldsymbol{\varepsilon}_T}{\partial T}\right)_{\boldsymbol{\tau}_\mathrm{app}}\right]
\end{aligned} \tag{19}
$$

With the analytical expression Eq. 14, 15, and 16, $\partial H_\mathrm{c}/\partial(-\hat{\sigma})$ and $\partial H_\mathrm{c}/\partial \boldsymbol{\tau}$ can be evaluated analytically at any stress state. Here we estimate the rest of the expression based on the following assumptions: First, the isotropic component refers to the thermal expansion effect (5),

$$\left[\left(\frac{\partial(-\hat{\sigma})}{\partial \boldsymbol{\varepsilon}_T}\right)\left(\frac{\partial \boldsymbol{\varepsilon}_T}{\partial T}\right)_{\boldsymbol{\tau}_\mathrm{app}}\right] = \frac{\partial P}{\partial T} = V\left(\frac{\partial P}{\partial V}\right)\cdot\frac{1}{V}\left(\frac{\partial V}{\partial T}\right) = K\alpha_V \tag{20}$$

where P is the hydrostatic pressure; α_V is the volumetric thermal expansion coefficient; and K is the bulk modulus. Second, the shear component expresses the thermal softening effect due to the decreasing shear modulus with increasing temperature (2), assuming that the shear modulus does not change significantly with temperature,

$$\left[\left(\frac{\partial \boldsymbol{\tau}}{\partial \boldsymbol{\varepsilon}_T}\right)\left(\frac{\partial \boldsymbol{\varepsilon}_T}{\partial T}\right)_{\boldsymbol{\tau}_\mathrm{app}}\right] = \left[\frac{\partial \boldsymbol{\tau}}{\partial T}\right]_{\boldsymbol{\varepsilon}_T} = \left[\frac{\partial(\mu\boldsymbol{\varepsilon}_T)}{\partial T}\right]_{\boldsymbol{\varepsilon}_T} = \boldsymbol{\varepsilon}_T\left(\frac{\partial \mu}{\partial T}\right)_{\boldsymbol{\varepsilon}_T} \approx \frac{1}{\mu}\left(\frac{\partial \mu}{\partial T}\right)_{\boldsymbol{\varepsilon}_T}\cdot\boldsymbol{\tau} \tag{21}$$

where μ is the shear modulus, and $(\partial\mu/\partial T)$ is the gradient of shear modulus respect to temperature. Combining Eq. 20 and 21 into Eq. 19, we reach the analytical model for predicting stress-dependent activation entropy Eq. 6. It is worth noting that the parameters we used here only includes the material's properties, without any fitting from direct MD simulations.

Note that the activation entropy contribution from the second term (Eq. 21) is relatively small comapred to the first term (Eq. 20). The activation entropy increases with increasing shear stress τ^* because both terms increases with τ^*. While it is readily seen that the second term increases with τ^*, the first term also increases with τ^*, as shown in Fig. S4(b)(c).

Figure 3 shows the comparison between the activation entropy (solid dots) from MEP calculations and the estimated values (dashed lines) from Eq. 18. The materials properties from the interatomic potential (6) are given as $K = 183\,\mathrm{GPa}$, $\alpha_V = 3.9 \times 10^{-5}\,\mathrm{K}^{-1}$, and $\mu = 81.4\,\mathrm{GPa}$. The gradient of the shear modulus as a function of temperature is obtained from molecular dynamics of perfect crystal (7) as $\partial\mu/\partial T = 1.77 \times 10^{-2}\,\mathrm{GPa}\cdot\mathrm{K}^{-1}$. The perfect agreement indicates that the activation entropy can be well explained by the thermal expansion and thermal softening effects in the HTST with constant applied stress $\boldsymbol{\tau}_\mathrm{app}$.

VI. The determinant method for calculating the product of harmonic vibrational frequencies

For the eigendecomposition of an *non-singular* matrix $\mathbf{K} = \mathbf{V}\mathbf{\Lambda}\mathbf{V}^T$, the eigenmatrix is $\mathbf{\Lambda} = \text{diag}(\{\lambda_i, i = 1, \ldots, 3N\})$, and the eigen-frequencies are $\nu_i \equiv \omega_i/2\pi = \sqrt{\lambda_i/m}/2\pi$. If we have the LU decomposition $\mathbf{K} = \mathbf{L}\mathbf{U}$, the product of the eigenvalues can be written as,

$$\prod_{i=1}^{3N} \lambda_i = \det(\mathbf{K}) = \det(\mathbf{L})\det(\mathbf{U})$$
$$= \prod_{i=1}^{3N}(L_i U_i) \qquad [22]$$

where L_i and U_i are the diagonal elements of the $\mathbf{L}$ and $\mathbf{U}$ matrices.

After the Hessian matrix is modified with Eq. 9 the resulting matrix $\mathbf{K}$ becomes non-singular, and the product of the eigen frequencies can be obtained by the determinant (LU decomposition),

$$\prod_{j=1}^{3} \lambda_j^k \cdot \prod_{i=1}^{3N-3} \lambda_i = \det(\mathbf{K}) \qquad [23]$$

where ν_j^k are the three eigen values corresponding to the added spring forces. It can be proved that the spring forces are independent to all the vibrational modes in the system. The modified matrix $\mathbf{K}'$ can be written as,

$$\mathbf{K}' = \mathbf{K} + k\tilde{\mathbf{I}}_3 \qquad [24]$$

where $\tilde{\mathbf{I}}_3 = \text{diag}(1, 1, 1, 0, \ldots, 0)$ is a diagonal matrix with only three 1's on the main diagonal. Since the diagonalization of $\mathbf{K} = \mathbf{V}\mathbf{\Lambda}\mathbf{V}^T$ satisfies $\mathbf{V}\mathbf{V}^T = \mathbf{I}$, we can write,

$$\tilde{\mathbf{I}}_3 = \mathbf{V}\tilde{\mathbf{I}}_3\mathbf{V}^T \qquad [25]$$

Therefore, the modified matrix can be eigendecomposed into,

$$\mathbf{K}' = \mathbf{V}(\mathbf{\Lambda} + k\tilde{\mathbf{I}}_3)\mathbf{V}^T \qquad [26]$$

It is proved that the eigenvalues corresponding to the added spring forces $\lambda_j^k = k$. The vibrational frequency term ν_{HTST} is then calculated by the ratio between the determinants of states A and S since the frequencies from the spring forces are cancelled out:

$$\nu_{\text{HTST}} = \frac{\prod_{i=1}^{3N-3} \nu_i^A}{\prod_{j=1}^{3N-4} \nu_j^S} = \frac{\prod_{i=1}^{3N-3} \frac{1}{2\pi}\sqrt{\lambda_i^A/m}}{\prod_{j=1}^{3N-4} \frac{1}{2\pi}\sqrt{\lambda_i^S/m}} = \frac{1}{2\pi}\sqrt{\frac{\det(\tilde{\mathbf{K}}_A) \cdot \lambda_-^S}{\det(\tilde{\mathbf{K}}_S) \cdot m}} \qquad [27]$$

where λ_-^S is the negative eigenvalue that is obtained directly using the 'eigs' method in MATLAB, and the determinant is calculated by LU decomposition in MATLAB. In this work, we select $k = 10^{-4}$ eV/Å to avoid round-off errors.

VII. Statistical estimation of the dislocation cross-slip rate and the effect of thermostat

Dislocation cross-slip is a thermally activated process which follows the Poisson's process [8]. The probability distribution function of the occurrence N is written as,

$$f(N) = \frac{(\lambda t)^N}{N!}\exp(-\lambda t) \qquad [28]$$

where t is the observation time, and the parameter λ represents the average occurance rate of the process.

We use MD simulations (See Methods) to obtain the estimate of the cross-slip rate, as shown in Fig. 1C and Fig. 2B. Our simulations start with a single screw dislocation in the slip plane, and stop when cross-slip occurs. Therefore, we are sampling the random variable observation time t at which the first cross-slip occurs (waiting time), equivalent to the Poisson's process with occurrence $N = 0$,

$$\tilde{P}(t) = f(N = 0) = \exp(-\lambda t) \qquad\qquad [29]$$

The rate parameter λ can be estimated using n independent MD simulations of the same applied stress and temperature conditions the maximum-likelihood estimator (MLE) $\hat{\lambda}_{\mathrm{MLE}} = 1/\sum_{i=1}^{n} t_{\mathrm{cs}}^{i}$, where t_{cs}^{i} is the cross-slip time of the i-th case. The 95 % confidence interval of the MLE can be approximately calculated as $\hat{\lambda}_{\mathrm{MLE}}(1 \pm 1.96/\sqrt{n})$ when the sample $n > 20$ (9).

To demonstrate this statistical treatment, we present new independent MD simulations at the applied stress $\boldsymbol{\tau}_{\mathrm{app}} = (-0.6, -0.8, 0.8)\,\mathrm{GPa}$ and different temperatures $T = 350, 400, 450, 500\,\mathrm{K}$ conditions in Fig. S6. The solid curve shows the exponential fitting curve using the MLE, and the dashed curves indicate the 95 % confidence interval. This errorbar of about 20% is very small and is not visible (smaller than the markers) on the log plot shown in Fig. 2 and Fig. S3. The width of the confidence interval shrinks with increasing number of independent numbers n, in consistency with the central limit theorem (9).

To demonstrate that the Nosé-Hoover thermostat (NVT ensemble) does not introduce additional thermal excitation and influence the thermally activated cross-slip, we performed additional 94 independent MD simulations of dislocation cross-slip without thermostat (NVE ensemble). We start from the same configuration that has been equilibrated at given stress and temperature conditions as the NVT simulations, and we then turn off the thermostat (NVE ensemble) so that the energy of the system is conserved. Fig. S6(b) shows the comparison of the 71 independent NVT simulations and the 94 independent NVE simulations, and it is readily shown that the NVE simulations has the same rate as the NVT simulations within the 95 % confidence interval. Fig. S6(c) shows the process of the two randomly selected cases from NVT and NVE simulations, respectively, which shows that the thermostat does not significantly influence the statistics of the system during the wait time of cross-slip.

It is worth noting that there is a small "incubation time" observed in the simulations, as is shown clearly in Fig. S6(a). This incubation time may be due to the insufficient time for decorrelating multiple MD trajectories generated from perturbing the same initial configuration. Even though the MD trajectories are chaotic, it would still take some time (i.e., the decorrelation time) for the trajectories to diverge from each other. In addition, there may be other causes, e.g., thermal equilibrium of vibrational modes. We opted to not shift the origin of the time axis to avoid hiding abovementioned effects. Instead, we simply lump such effects in the error bars of the rate estimate, which are sufficiently small for our purposes. We also wish to point out that the incubation time effect is hardly visible in lower temperature simulations shown in Fig. S6(b-d), where the average cross-slip time is much longer compared to the decorrelation time.
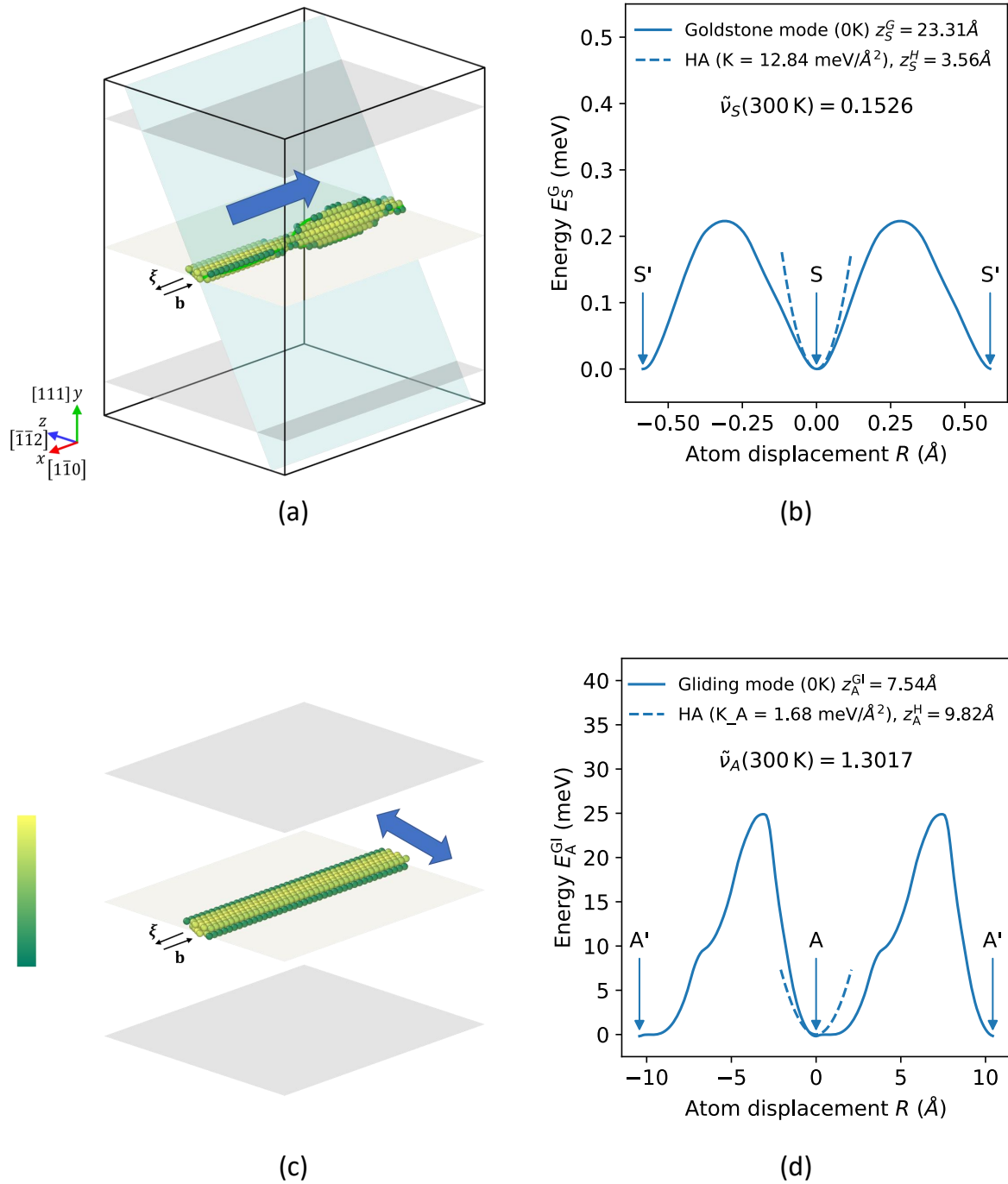
Supporting Figures and Tables

Fig. S1. Soft vibrational modes and their energy profiles. (a) Goldstone mode of the activated state S, where the constrictions can move along the dislocation line. (b) Energy profile of the Goldstone mode and its harmonic approximation at the activated state. The horizontal axis is the total atomic displacement. (c) Gliding mode of the initial state A, where the dislocation can glide along the original slip plane. (d) Energy profile of the Gliding mode and its harmonic approximation. The horizontal axis is the total atom displacement.
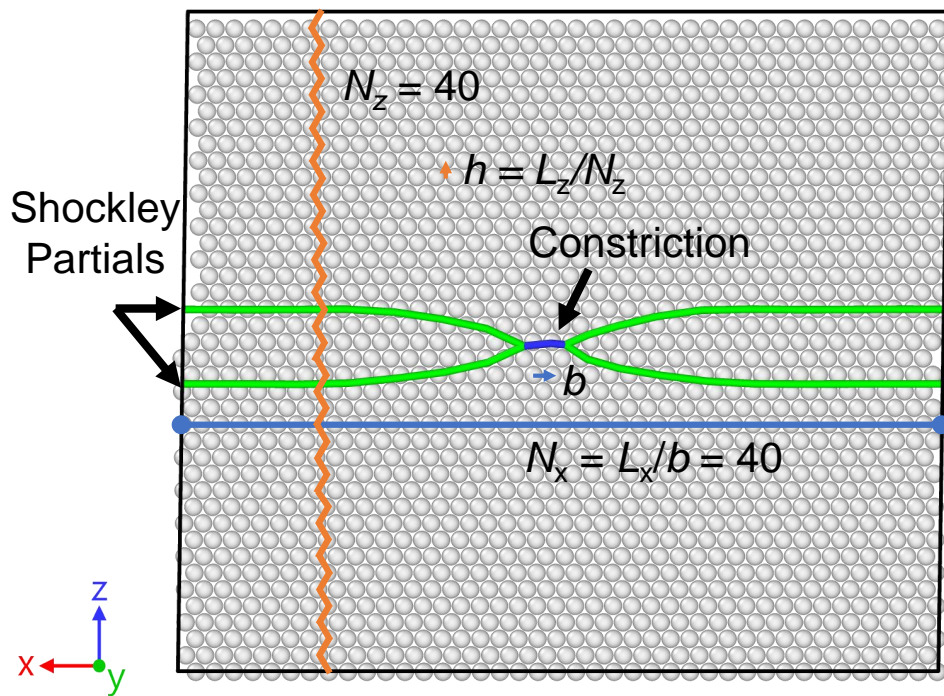
Fig. S2. Schematics of the repeated periods in the simulation cell's x (Goldstone mode) and z (Gliding mode) directions. The Goldstone mode is defined as the constriction motion along the dislocation line direction, with the repeated distance of $b = 2.49\,\text{Å}$, the magnitude of the Burger's vector, and repeated period $N_x = 40$. The Gliding mode is defined as the dislocation motion in the original slip plane, with the repeated distance of $h = 2.16\,\text{Å}$, and repeated period $N_z = 40$.
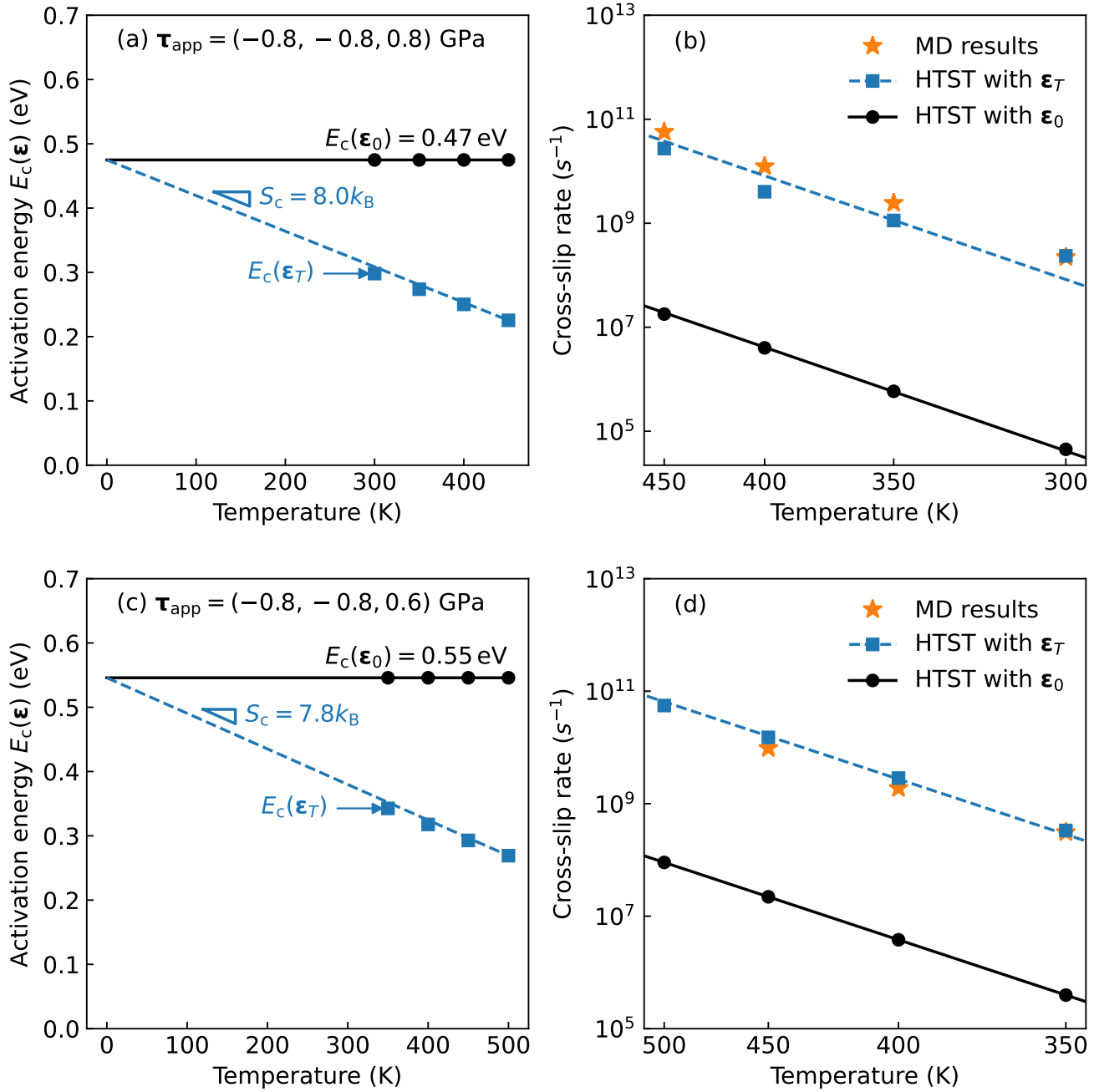
Yifan Wang and Wei Cai

Fig. S3. MD simulations and MEP calculations for additional applied stress conditions. (a) Activated energy calculated at zero-temperature strain ε_0 and corresponding finite-temperature strain ε_{T} for $\boldsymbol{\tau}_{\mathrm{app}} = (-0.8, -0.8, 0.8)\,\mathrm{GPa}$. (b) Estimated rates using HTST (Eq. 4) with the activation energy and prefactor evaluated at ε_0 and ε_{T}. (c) Activated energy results and (d) Estimated rate results for the applied stress of $\boldsymbol{\tau}_{\mathrm{app}} = (-0.8, -0.8, 0.6)\,\mathrm{GPa}$. The benchmark MD rates are performed for four temperature conditions ($T = 350, 400, 450, 500\,\mathrm{K}$) in (b) and three temperature conditions ($T = 350, 400, 450\,\mathrm{K}$) in (d), shown as the orange stars with error bar.
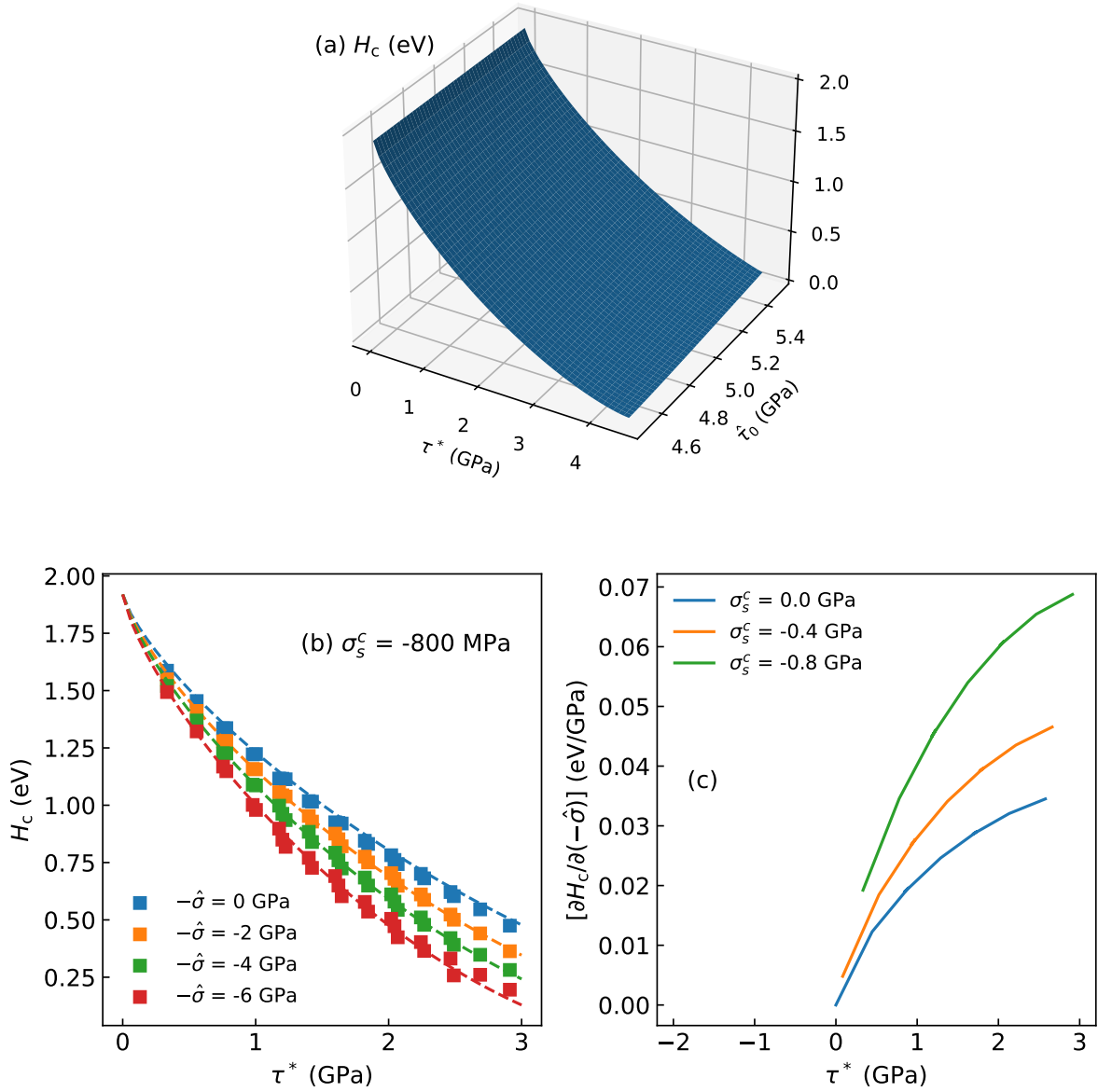
Fig. S4. (a) Stress-dependent activation enthalpy. Activation enthalpy estimated from Eq. 14 as a two-dimensional function of τ^* and $\hat{\tau}_0$. (b) Activation enthalpy H_c as a function of effective shear stress τ^* at different isotropic stresses (negative pressure) $(-\hat{\sigma})$. (c) Derivative of the activation enthalpy over the isotropic stress $[\partial H_c / \partial(-\hat{\sigma})]$ as a function of τ^*.
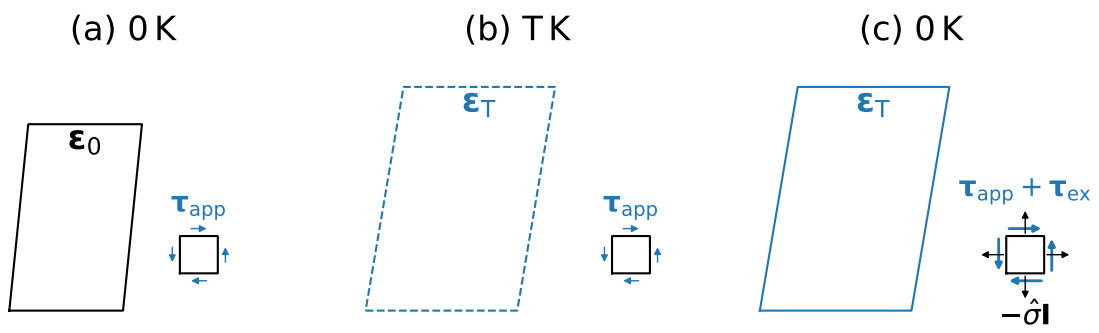
Fig. S5. Thermal expansion and thermal softening effects. (a) Zero-temperature strain state ε_0, with fixed applied stress τ_{app}. (b) Finite-temperature strain state ε_{T}, with fixed applied stress τ_{app}. (c) Negative isotropic stress $-\hat{\sigma}\mathbf{I}$ and excess shear stress τ_{ex} are needed for reaching the finite-temperature strain state ε_{T} at $0\,\mathrm{K}$.
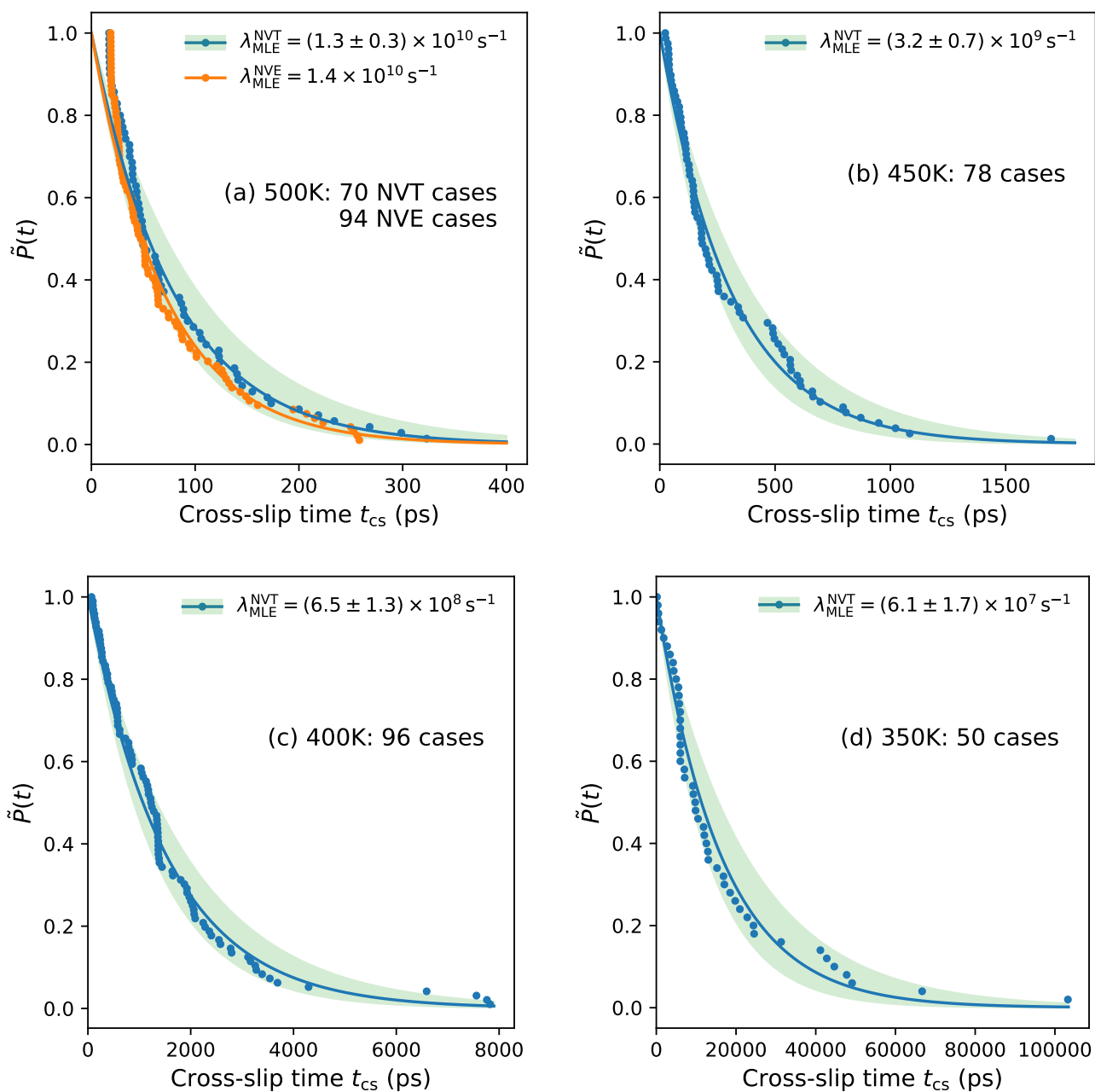
Fig. S6. Fraction $\tilde{P}(t)$ of configurations that have not cross-slipped as a function of t for applied stress of $\boldsymbol{\tau}_{\mathrm{app}} = (-0.6, -0.8, 0.8)\,\mathrm{GPa}$, at temperature of (a) $500\,\mathrm{K}$, (b) $450\,\mathrm{K}$, (c) $400\,\mathrm{K}$, (d) $350\,\mathrm{K}$. The solid blue line is the fitted exponential distribution using the maximum-likelihood estimator (MLE) λ_{MLE} using the new NVT simulations (blue dots), and the green filled region shows the $95\,\%$ confidence interval of the estimator. The solid orange line and dots in (a) presents the simulations without thermostat (NVE ensemble), to demonstrate that the Nosé-Hoover thermostat (NVT ensemble) does not introduce additional thermal excitation and influence the thermally activated cross-slip, see SI Text VII.

Table S1. Fitting parameters for Eq. 14, 15, and 16

$C_{\mathrm{e}}^{\mathrm{g}}$	-2.1077
$C_{\mathrm{e}}^{\mathrm{c}}$	1.1150
$D_{\mathrm{s}}^{\mathrm{c}}$	0.7218
A	1.9193
p	0.7711
q	1.4428
τ_0	5.5949
K_1	0.1592
K_2	0.3620
K_3	0.6994

References

1. L Proville, D Rodney, MC Marinica, Quantum effect on thermally activated glide of dislocations. *Nat. materials* **11**, 845–849 (2012).
2. S Ryu, K Kang, W Cai, Predicting the dislocation nucleation rate as a function of temperature and stress. *J. Mater. Res.* **26**, 2335–2354 (2011).
3. WP Kuykendall, Y Wang, W Cai, Stress effects on the energy barrier and mechanisms of cross-slip in FCC nickel. *J. Mech. Phys. Solids* **144**, 104105 (2020).
4. G Esteban-Manzanares, R Santos-Güemes, I Papadimitriou, E Martínez, J LLorca, Influence of the stress state on the cross-slip free energy barrier in Al: An atomistic investigation. *Acta Materialia* **184**, 109–119 (2020).
5. Y Mishin, MR S(/)rensen, AF Voter, Calculation of point-defect entropy in metals. *Philos. Mag. A* **81**, 2591–2612 (2001).
6. S Rao, TA Parthasarathy, C Woodward, Atomistic simulation of cross-slip processes in model fcc structures. *Philos. Mag. A* **79**, 1167–1192 (1999).
7. G Clavier, et al., Computation of elastic constants of solids using molecular simulation: comparison of constant volume and constant pressure ensemble methods. *Mol. Simul.* **43**, 1413–1422 (2017).
8. G Esteban-Manzanares, B Bellón, E Martínez, I Papadimitriou, J LLorca, Strengthening of Al–Cu alloys by Guinier–Preston zones: Predictions from atomistic simulations. *J. Mech. Phys. Solids* **132**, 103675 (2019).
9. V Guerriero, Power law distribution: Method of multi-scale inferential statistics. *J. Mod. Math. Front.* **1**, 21–28 (2012).